Eur. Phys. J. B **49**, 147–155 (2006)
DOI: 10.1140/epjb/e2006-00039-7

THE EUROPEAN PHYSICAL JOURNAL B

Diffraction of oriented nano-peapods

R. Almairac[1,a], J. Cambedouzou[1], S. Rols[1], and J.-L. Sauvajol[1]

Laboratoire des Colloïdes, Verres et Nanomatériaux (UMR CNRS 5587), Université Montpellier II, 34095 Montpellier Cedex 5, France

Received 14 April 2005 / Received in final form 14 December 2005
Published online 17 February 2006 –

Abstract. This paper presents an investigation of the structural properties of oriented A@SWNT peapods, where A represents any molecular species organized on a 1D cristalline chain inside the single wall nanotubes (SWNT). This study is based on the use of diffraction methods applied to the case of oriented A@SWNT samples. Two preferential orientations of tubes are considered, 1D (fiber) and 2D (pellet) both having an axial symmetry. We show that even in the case of samples presenting a very large mosaic, information about the correlation state between C_{60} chains and about the C_{60} polymerization, can be obtained provided that pertinent scans are performed. These are longitudinal scans along and perpendicularly to the symmetry axis accompanied by convenient constant Q scans. Detailed diffraction patterns are simulated in the case of a 2D oriented sample of C_{60}@SWNT peapods ('bucky paper').

PACS. 61.46.+w Nanoscale materials: clusters, nanoparticles, nanotubes, and nanocrystals – 61.48.+c Fullerenes and fullerene-related materials – 61.10.Nz X-ray diffraction

1 Introduction

A large variety of insertion compounds have been made with single-walled carbon nanotubes (SWNTs) since their discovery in 1991 [1]. Insertion of ions or molecules in SWNTs or in bundles of SWNTs generally results in a modification of their electronic properties [2], opening the way to interesting potential applications. Very different molecules have been successfully inserted, generally by filling the hollow cavity of the tubes [3]. Once synthesized, the characterization of the new compound is very often made by high resolution transmission electron microscopy (HRTEM). It provides a 'direct' imaging of the local structure of filled SWNTs and it very often shows the way the molecules do order inside the tubes. Numerous examples of insertion compounds are given by the so-called 'peapods' of SWNT. The terminology used to describe these structure is A@SWNT where A stands for a molecule, an ion or an atom inserted inside the hollow cavity [3] of the tube. A remarkable representative member of these complex molecular species is the C_{60}@SWNT peapod. In this compound, the fullerene molecules are regularly spaced along the nanotube axis so as to form a confined 1D crystal.

Direct imaging by HRTEM is essential to the knowledge of the structural organization of these compounds. However, in the case of fullerene based SWNT peapods, it has been shown that electronic beam irradiation results in small damages or perturbations of the local molecular and atomic order as it can produce displacement of C_{60} molecules, dimerization or cluster formation of $(C_{60})_n$ inside the tubes [3–5]. Other techniques allowing the A@SWNT samples to be characterized at a macroscopic level exist. X-ray and neutron diffraction probe from μm^3 to mm^3 sample size without inducing any damage to the molecular structure of the peapods. These methods give complementary information to those derived from HRTEM. In particular, statistical information (distribution of tube diameter, lattice parameter etc.) and global orientation of the tubes (mosaic angle etc.) are easily achieved using diffraction while unreachable using direct local methods.
This paper deals with the application of diffraction methods to the study of the structural organization of C_{60}@SWNT peapods. Two questions are still open for which HRTEM could not give definitive answers.

The first question concerns the ordering of C_{60} molecules along the tubule. Results from diffraction experiments provide a C_{60}–C_{60} statistical distance of ∼0.97 nm [6–9] which is lower than the distance in C_{60} fcc crystals — of 1.00 nm — and significantly higher than the polymerized C_{60}–C_{60} distance given in the literature (0.92 nm). This suggests that the C_{60} molecules inside a tubule could be partly dimerized or polymerized. However long chains of regularly spaced molecules with a coherence length of ∼40 peas have been deduced from a diffraction data analysis [6]. More recently a Tight Binding Molecular Dynamics simulation of the most stable structure of C_{60}@SWNT

[a] e-mail: almairac@gdpc.univ-montp2.fr

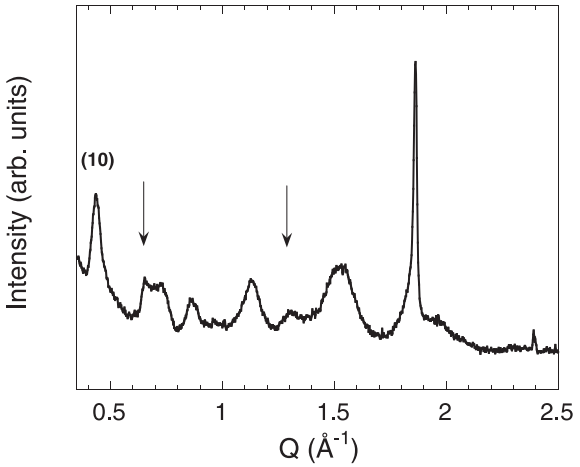

Fig. 1. Diffraction pattern of a powder of C_{60}@SWNT peapods. The (10) peak is due to the array of tubes and the arrows indicate the signal of C_{60} 1D crystals at 0.65 and 1.3 Å^{-1}. The peak at 1.87 Å^{-1} is due to graphite impurities.

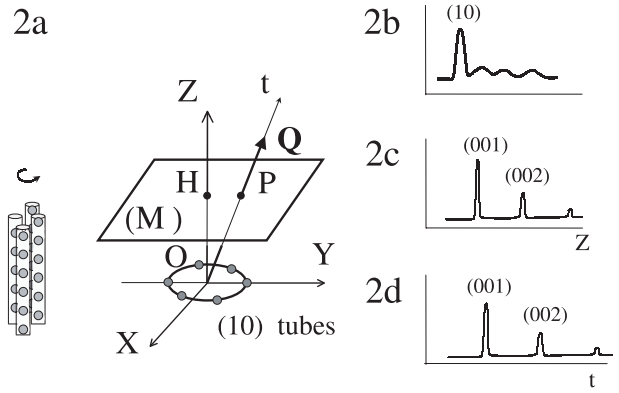

Fig. 2. 1D oriented C_{60}@SWNT sample. Left part of (a) bundle in direct space, right part: corresponding reciprocal space. (b), (c) and (d) are schematic representations of scans along lines passing through the origin. Scan in (XOY) plane: (b), along OZ: (c) and along Ot: (d).

peapods support a dimerized structure which is calculated to be energetically very favorable [10]. These different results demonstrate that the ordering of C_{60} inside SWNTs is not yet completely understood.

The second question concerns the correlation between C_{60} molecules belonging to different tubes inside the same bundle. As we shall detail further in this paper, in the absence of correlation, the C_{60} crystals are perfectly 1D. However, if some structural correlation exists as suggested by recent HRTEM studies in (Ca@C_{82})@SWNT peapods [5], 3D nano-crystals of C_{60}@SWNT are formed. The physical properties of these two types of peapods are supposed to be different. Therefore, the coherence length of these crystals inside a bundle, i.e. the number of nanotubes concerned, plays an important role in the physics involved in this molecular system.

In this work we present calculations of the diffraction pattern of C_{60}@SWNT peapods in the case of oriented samples. The calculation method of the diffraction pattern for a *powdered*, i.e. isotropic sample, has been reported previously [6,11]. In that case, experimental data and calculated patterns both display C_{60} characteristic peaks, demonstrating fullerene ordering inside the tubules, but these peaks are embedded into the SWNT bundle signal (see Fig. 1). In a recent paper, Zhou et al. [12] have presented diffraction results obtained on a 'paper' of C_{60}@SWNT peapods. They have shown that the partial 2D orientation of the SWNT strongly modify the diffraction diagram. The aim of the present paper is to define a method of structural analysis based on the calculation of the diffraction diagram of *oriented* peapods samples. In such a case we will show that the C_{60} signal is separated — or easy to separate — from that of the SWNTs bundles.

Our paper is organized as follows: in Section 2 we present an intuitive description of the diffraction patterns in the case of oriented SWNT peapods so as to introduce the method used for the simulations. We begin with a 1D perfectly oriented sample followed by the 2D oriented sample case. Section 3 gives a detailed description of the numerical model used for the simulations of the diffraction patterns. Different experimental settings for the diffractometer are considered. In the discussion (Sect. 4) we apply the simulations to a 2D mosaic sample — a 'paper' of C_{60}@SWNT peapods — with various mosaic angles. We also consider the use of an image plate detector with an oriented peapods sample.

2 The diffraction patterns of oriented samples

This first part stands as a comprehensive introduction to the numerical simulations that will be presented in Section 3. Therefore, only schematic diffraction patterns are presented in this section.

2.1 1D oriented C_{60}@SWNT samples

Let consider a sample consisting of a large number of bundles of C_{60}@SWNT peapods, all having their long axis oriented vertically. The 2D triangular lattice formed by the tubes is chosen to have a random orientation around the vertical axis. In Figure 2a the left part represents a bundle in direct space and the right part represents the corresponding reciprocal space. In the following we consider only small Q signal, i.e. Q values lower than 2 Å^{-1}, so that the discrete carbon atoms of tubes and C_{60} can be replaced by a uniform scatterer density. In the reciprocal space the response of the 2D lattice of infinitely long bundles is *strictly* restricted to the horizontal (XOY) plane. This is illustrated by the (10) reflections that give 6 dots per bundle. These dots are replaced by a circle when accounting for all possible orientations of the bundles around

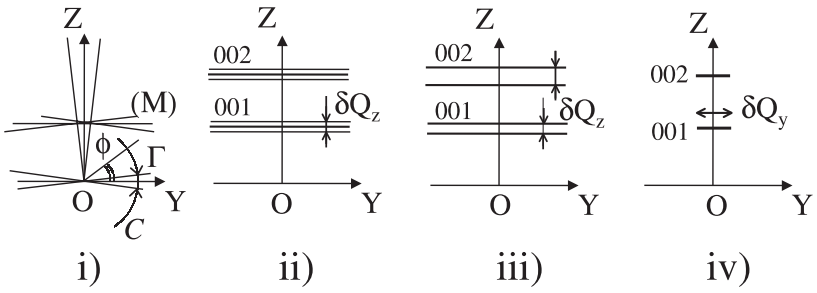

Fig. 3. Imperfect 1D C_{60}@SWNT sample: reciprocal space. i) Mosaic effect and definition of the angle ϕ; ii) short chain effect; iii) dispersion of the parameter; iv) correlation between C_{60} chains.

the vertical axis. The other (hk) reflections of the 2D lattice give also circles lying in the (XOY) horizontal plane (not represented). In the case where there is no correlation between the C_{60} chains of different tubes (this assumption may be justified by the different chiralities of the tubes forming the bundles), each 1D crystal is perfect and the corresponding reciprocal space is made of successive parallel planes at $Z = 0$, $Z = 2\pi/d$, ..., $Z = 2\pi l/d$ where l is an integer and $d = 0.97$ nm is the C_{60}–C_{60} distance in the C_{60} 1D crystal. These planes will be noted $(00l)$ and called (M) planes. Within each plane the response is continuous, modulated by some form factor. We can observe that the sample itself and its reciprocal space present an axial symmetry around Oz.

Three circles or four circles diffractometer can follow any path in the reciprocal space, the scattering vector of which is called $\boldsymbol{Q}$. As usual one has $Q = 4\pi \sin\theta/\lambda$, where λ is the wavelength of the incident beam. Figure 2b illustrates a scan along any direction along the (XOY) plane. Only the 2D lattice of the tubes gives a response when scanning this plane. In Figures 2c and 2d we give an illustration of the diffraction for scans along the OZ direction and along an oblique direction starting from the origin. The two patterns look similar but are not identical: they contain the same $(00l)$ peaks but at different values of Q. This example illustrates the unusual behavior expected for a 1D perfect crystal, i.e. the peak position depends on the orientation of $\boldsymbol{Q}$. Therefore, for such 1D oriented samples, the C_{60} response can be observed separately from that of the bundles. One has to account for these peculiar 1D effect when interpreting the diffraction diagram of — at least partly — 1D ordered samples. This could be of major importance for peapods fibers for example. However, these 1D fiber-like systems are likely to be far from this perfect model. Therefore imperfections have to be introduced in the model. Four effects will be considered: i) mosaic; ii) finite length of the C_{60} chains; iii) distribution of the chain parameter d; and iv) correlation of C_{60} chains between adjacent tubes. We assume that the radial symmetry is preserved so that all figures can be made in the (YOZ) plane. Appropriate scans can estimate each effect assuming that the intensity follows some distribution law for which we take Gaussian functions for simplicity.

i) In a mosaic sample the bundle axis direction follows such an angular distribution law. The mosaic angle — the full width at half maximum (FWHM) of the distribution- can be determined by measuring the bundle signal along the C line (constant Q scan along a circle as shown in Fig. 3i). The diffracted intensity is then plotted as function of the angle ϕ. If the mosaic angle Γ is not too large the intensity can be written $I(\phi) = I_0 e^{-\alpha\phi^2}$ with $\Gamma = 2\sqrt{\ln 2/\alpha}$. In the case of a large mosaic angle ($\Gamma > \sim 70°$), one has to take account of the periodicity of $I(\phi)$. In such a case, as the periodicity is 180°, the correct expression becomes $I(\phi) = I_0 \sum_i e^{-\alpha(\phi - 180\, i)^2)}$ where i is an integer.

ii) If the C_{60} chains are short (made of few molecules), the finite size effect has the consequence to replace the infinitely thin (M) planes by planes with a non-zero thickness. In the diffraction diagram, these planes give broad responses, the half width of which δQ_z is related to the coherence length along the chain by $L \sim 2\pi/\delta Q_z$. In this case all $(00l)$ planes present the same width which can be estimated by doing $\boldsymbol{Q}$ scan along the Oz direction in the reciprocal space (Fig. 3ii).

iii) A disordered chain will present a dispersion of the parameter of the chain d. As an example, let consider an inhomogeneous chain of C_{60} made of two parts, the first being equally spaced fullerenes ($d \sim 10$ Å) and the second being polymerized C_{60} ($d \sim 9.2$ Å). The total signal is the sum of two signals of the 1D crystals with two different parameters d. The distance between the two corresponding (M) planes $(00l)$ increases like l. The case of continuous dispersion of the parameter is schematically shown in Figure 3iii. For this case, the half width δQ_z of the (M) $(00l)$ planes depends on the l index. The dispersion of the parameter is $\delta d \sim 2\pi * l/\delta Q_z$, with δQ_z measured along the Oz direction in the reciprocal space. Cases (ii) and (iii) are easily distinguishable by their l dependency.

iv) Let suppose that correlations exist between the different chains of C_{60} inside a bundle, giving rise to a 3D nano-crystal of parallel C_{60} chains. As the 1D character is lost each (M) plane reduces to a disc whose diameter δQ_y gives the correlation length perpendicularly to the nanotubes axis. This correlation length $L \sim 2\pi/\delta Q_y$ can be measured along each (M)

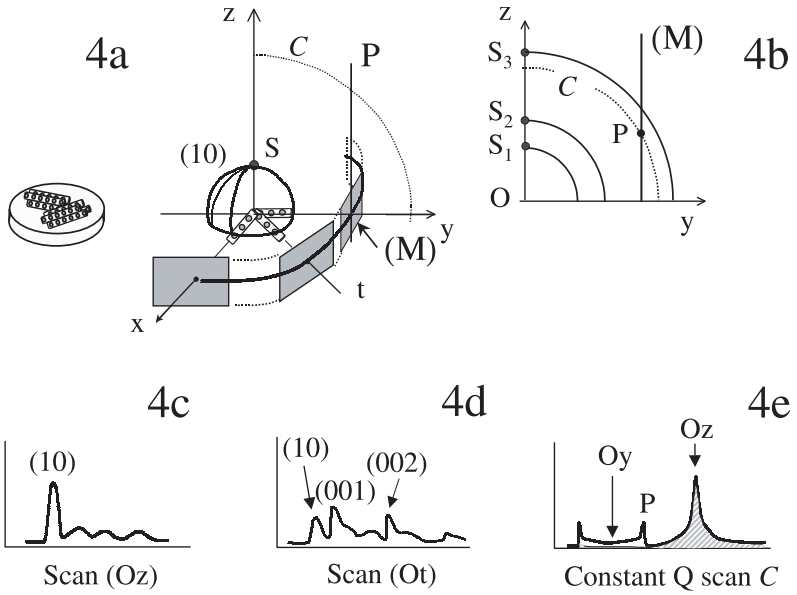

Fig. 4. 2D oriented C_{60}@SWNT sample. Left part of (a): bundles in direct space, right part: corresponding reciprocal space. (b): details of plane (yOz); (c), (d) and (e) are schematic scans along Oz, Ot and along the C curve, respectively.

plane along the (OY) direction in the reciprocal space (Fig. 3iv). In that case δQ_y does not depend on the plane index l. Note that if 3D correlation are strong enough, new additional reflections could appear inside each (M) plane, but they would remain very weak.

Presumably, a 1D oriented sample of C_{60}@SWNT peapods would contain the four effects simultaneously. Consequently the expression of the intensity $I(\boldsymbol{Q})$ must take into account the four Gaussian distributions.

However, no experimental work dealing with a real 1D oriented C_{60}@SWNT peapod sample has ever been published, excepted for electron diffraction [13]. Therefore we will consider the different aspects of a 2D oriented sample, an example of which is frequently found experimentally as a 'paper' or 'mat' sample [12].

2.2 2D oriented C_{60}@SWNT samples

First let consider a perfect pellet (or a film) of peapods. We orient the pellet horizontally so that all the bundles lay within the horizontal plane with an homogeneous angular distribution around the (Oz) axis (Fig. 4a left). The reciprocal space of this sample is obtained by repeating the construction of Figure 2a for each bundle orientation (Fig. 4a right). It comprises two parts:

1) The 2D (hk) reflections from the bundles lattice are contained on spheres with a maximum signal at the S point on the vertical Oz axis. The reason for this maximum is that all the bundles of the pellet are simultaneously in reflection at this point [14] . Moreover to take into account the very large width of the (hk) reflections (along a radius, see Fig. 1), one must consider that each sphere presents a non-zero thickness. As a consequence the 2D tube lattice signal is never extinguished whatever the point in the reciprocal space is.
2) The (00l) response is now made of all the (M) planes lying tangentially to a cylindric surface whose axis is parallel to Oz. Both the direct and reciprocal spaces possess a symmetric axial axis along Oz, so that the figure can be drawn in a plane (Fig. 4b).

A $\boldsymbol{Q}$ scan along Oz gives the (hk) reflections of the tube lattice and no signal from the (M) planes (Fig. 4c). Scans along any other direction give a mixture of the response of tube lattice and of the 1D C_{60} crystal (Fig. 4d), resembling to the powder diagram of Figure 1. Let now consider a constant Q scan along a circle C (Fig. 4b). If $Q \geq 2\pi/\mathrm{d}$, each time the current point goes across the (M) plane as shown by the point P, a maximum is expected (Fig. 4e). In this scan the bundle lattice signal, which becomes maximum when crossing the Oz direction, is very smooth and can be easily parametrized. Therefore, it can be easily subtracted from the total response, revealing the signal of the C_{60} crystal alone.

In Section 3, we present the simulation of the diffraction patterns for a 2D oriented sample, and will discuss in Section 4 the effects of mosaic, distribution of diameter, finite size and correlation in between C_{60} chains.

3 Simulations of the diffraction patterns for a 2D oriented sample

The simulated patterns presented in this section concern the perfect pellet of Section 2.2. In Appendix A we present the Ewald construction as a support to the interpretation of results obtained from calculation.

3.1 The measured signal

The signal measured by a diffractometer $I_m(\boldsymbol{Q})$ is the convolution product of the theoretical signal $I_{th}(\boldsymbol{Q})$ by the resolution function $R(\boldsymbol{Q})$ of the apparatus

$$I_m(\boldsymbol{Q}) = \int\int\int I_{th}(\boldsymbol{Q_1}) R(\boldsymbol{Q} - \boldsymbol{Q_1}) d^3Q_1 \qquad (1)$$

$I_{th}(\boldsymbol{Q})$ is the response drawn in reciprocal space ($\boldsymbol{Q}$ space) in Figures 2a and 4a. For a collection of bundles oriented along OZ as shown in Figure 2a, $I_{th}(\boldsymbol{Q})$ is given by [11]

$$I_{th}(\boldsymbol{Q}) = \frac{2\pi}{Q^2}\left[F_L^2\left(\sum_{i,j} B(s_{ij}Q_H)\right)\delta(Q_z) + F_C^2 \sum_{n\neq 0} p^2 \delta\left(Q_z - \frac{2\pi n}{d}\right)\right] \qquad (2)$$

where F_C and F_L (form factors along and perpendicularly to the tube axis, respectively) are given by

$$F_L = \rho L\, B(\rho Q_H) \frac{\sin\frac{Q_z d}{2}}{\frac{Q_z d}{2}} + a_C\, p \qquad (3)$$

and

$$F_C^2 = 2\pi N_T\, a_C^2. \qquad (4)$$

In these expressions we make the assumption of infinitely long tubes containing infinitely long C_{60} chains with no correlation between them. The case of correlated chains is studied in Section 4. $\rho = 0.68$ nm is the tube radius, d is the C_{60}–C_{60} distance inside a tube ($d \sim 0.97$ nm is the parameter of the C_{60} 1D crystal), a_C is equal to $(4\pi\rho_C^2(\sin Q\rho_C/Q\rho_C))$ where ρ_C is the C_{60} radius, p is the filling rate for which we take $p = 1$ and N_T is the number of tubes in the bundle. The $\boldsymbol{Q}$ vector has two components: Q_z along Oz and Q_H is the component lying in the plane perpendicular to the (bundle) tube axis. $B(\rho Q_H)$ and $B(s_{ij}Q_H)$ are two zero order Bessel functions and s_{ij} represents the distance between two different tubes (referred as tube i and tube j) in one bundle. In the case of a pellet, one has to take into account all the bundle orientations along the pellet plane. The expression (2) is then integrated over all the orientations:

$$I_{th}^{pellet}(\boldsymbol{Q}) = \int\int I_{th}(\boldsymbol{Q}) F(\boldsymbol{\Omega}) d\boldsymbol{\Omega} \qquad (5)$$

where $I_{th}(\boldsymbol{Q})$ is given by equation (2), $\boldsymbol{\Omega}$ is the solid angle, and $F(\boldsymbol{\Omega})$ defines the sample organization. More precisely in the case of the pellet (see Fig. 4a) one has $F(\boldsymbol{\Omega}) = 1$, if $\boldsymbol{\Omega}$ lies along the horizontal plane and 0 otherwise. Using equations (5) and (1) one obtains the measured intensity $I_m(\boldsymbol{Q})$.

The resolution function $R(\boldsymbol{Q})$ is commonly represented by a Gaussian function in the 3 dimensional $\boldsymbol{Q}$ space. It can be viewed as some volume for which the signal is transmitted. This volume is a small portion of the Ewald sphere. Consequently, it is often a very flat volume which can be imaged by a disc in the $\boldsymbol{Q}$ space. For an usual 3D crystal, the anisotropy of $R(\boldsymbol{Q})$ has only small effects on the diffraction pattern. But in the case of a 1D crystal for which the response is made of planes ((M)), the application of (1) can result in unexpected behavior of the measured signal $I_m(\boldsymbol{Q})$. The resolution parameters used for the simulations were adjusted on the measured patterns obtained for several samples with the powder diffractometer giving the diagram in Figure 1 (2θ diffractometer with a germanium (111) monochromator).

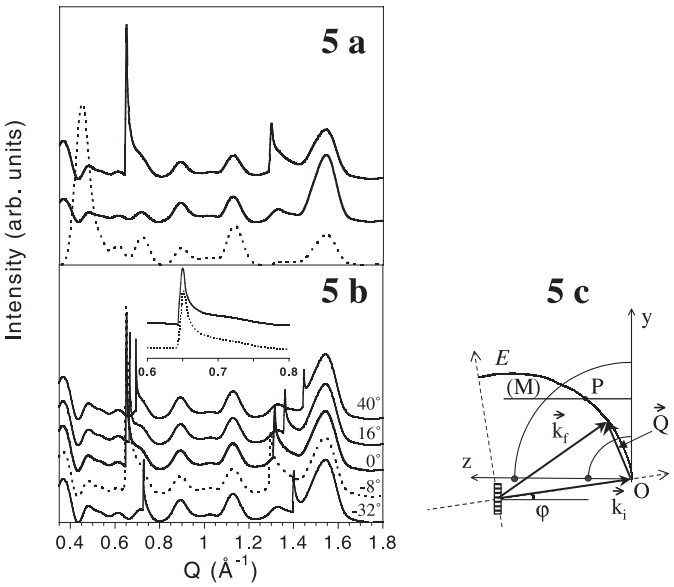

Fig. 5. Simulated patterns for a 2D oriented sample. (a) Scans along Oz and Oy (see Fig. 4); top curve: filled tubes along Oy; middle curve: filled tubes along Oz; dotted curve: empty tubes along Oy. (b): "2θ" scans in transmission for different orientations of the sample around $\varphi = 0°$, i.e. from bottom to top $-32°$, $-8°$, $0°$, $16°$ and $40°$. Inset: dotted curve for $\varphi = -8°$, continuous curve for scan Oy. (c) Shows the path E followed in reciprocal space for the scans of (b). For clarity only one (M) plane has been represented.

3.2 Usual 2θ and $\theta/2\theta$ scans

First we present results obtained for scans along lines in $\boldsymbol{Q}$ space that we will refer as 'longitudinal' in the following discussion. These lines start at the origin and keep a constant direction in the reciprocal space. We use the referential of the pellet given in Figure 4a. Three scans are shown in Figure 5a: a scan along Oy for empty tubes, a scan along Oy for filled tubes and a scan along Oz for filled tubes. These scan are performed in "$\theta/2\theta$" mode. Taking the Oz scan as example, the incident beam is parallel to the pellet surface at $Q = 0$, then the sample performs a rotation of θ when the detector rotates of 2θ (see Fig. 8a). As already observed [6,11] the intensity of the (10) reflection at $Q = 0.45$ Å^{-1} is strongly reduced for the filled tubes scans which are very similar up to $Q = 0.6$ Å^{-1}.

By contrast, the sharp peaks arising at $Q = 0.66$ Å^{-1} and at $Q = 1.3$ Å^{-1} when Q goes across the first and second (M) planes, do not appear in the Oz scan (middle curve) as explained before. We note that the maximum of the peak is limited by the resolution of the diffractometer for this perfectly oriented sample.

In Figure 5b "2θ" scans for which only the detector is turned during the data acquisition, are presented. In that case the path of the scattering vector $\boldsymbol{Q}$ in the reciprocal space is a circle E lying on the Ewald sphere as represented in Figure 5c. The incident and reflected beams are represented by the vectors $\boldsymbol{k_i}$ and $\boldsymbol{k_f}$ respectively. One has $\boldsymbol{Q} = -\boldsymbol{k_i} + \boldsymbol{k_f}$, $|\boldsymbol{k_i}| = |\boldsymbol{k_f}|$ and $2\theta = (\boldsymbol{k_i}, \boldsymbol{k_f})$. The incident beam is always perpendicular to the Ewald sphere at the origin O, and the angle φ between $\boldsymbol{k_i}$ and the perpendicular to the pellet (Oz) can take different values (see also Fig. 8a and Appendix A). When the pellet is oriented in a transmission geometry ($\boldsymbol{k_i}$ parallel to Oz, $\varphi = 0°$) one obtains a pattern resembling to the longitudinal scan along Oy (Fig. 5a top), but with a narrower (001) peak. Several patterns have been simulated for different φ angles ranging from $-40°$ to $40°$. The inset shows that the $\varphi = -8°$ orientation (dotted curve) is the most resembling to the longitudinal Oy scan. The (001) peak position strongly depends on the angle φ for the same reasons than those discussed for the oblique Ot line in Section 1. Consequently the correct C_{60}–C_{60} parameter measurement has to be done with the longitudinal Oy scan ("$\theta/2\theta$" mode). One has $d = 2\pi/Q_0$ where Q_0 corresponds to the sharp increasing side of the (001) peak in this case. The other determinations of d using 2θ scans are only approximate. However the error made on d is less than 0.01 nm if $-12° \leq \varphi \leq 6°$ in the 2θ operating mode.

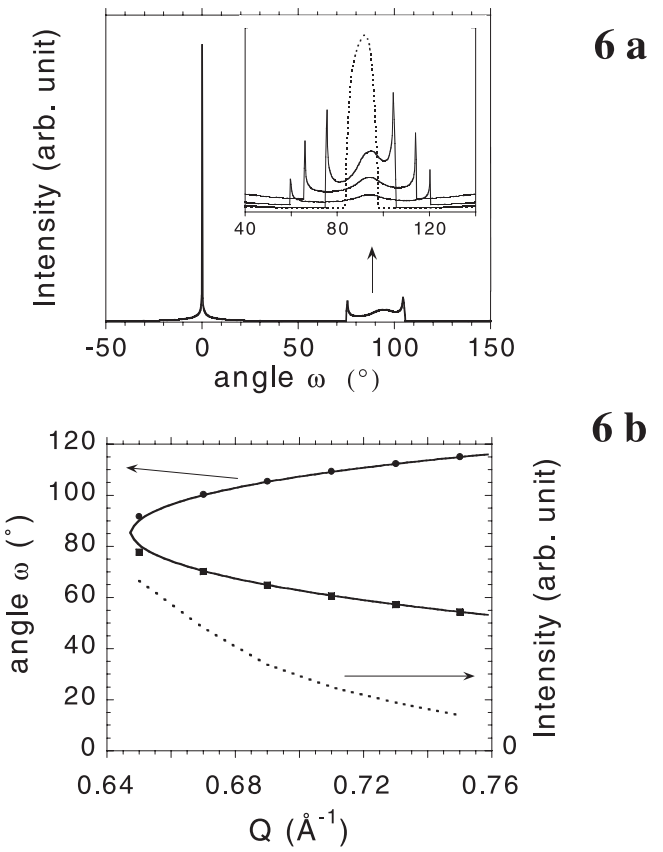

Fig. 6. Constant Q scans for a 2D oriented sample. (a) Constant $Q = 0.67$ Å^{-1} scan; inset: details for $Q = 0.65$ (central), 0.67, 0.71 and 0.75 Å^{-1} . (b) Peak position (continuous curve) calculated from a geometrical construction, dots and squares taken from the peaks in (a) and integrated intensity (dashed curve) of the (M) plane (001) signal as function of Q.

3.3 Constant Q scans

All the peapods scans presented in Figure 5 contain some mixture of tube lattice response and C_{60} crystal response. In the following we consider constant Q scans as described in Section 2.2, for different values of Q (Fig. 4e). The scanning variable is the angle φ or more conveniently $\omega = \varphi - 90° - \theta$, with θ kept constant (like Q — see Appendix A). The signal is periodic with a period of 180°. The scan displayed in Figure 6a has been calculated for $Q = 0.670$ Å^{-1}, i.e. for a Q value slightly above the limit value of 0.648 Å^{-1} for which the circle of the constant Q scan is precisely tangential to the (001) (M) plane. For the angle $\omega = 0°$ which corresponds to Q along the Oz axis, the signal originating from the tube lattice is maximum, all bundles being in reflection for this configuration as explained in Section 2.2. By contrast, this response is very small at $\omega = 90°$. We note that the sharpness of the peak at 0° is resolution limited. Each time the resolution goes across a (M) plane a sharp peak arises as shown by the two peaks at 75.67° and 104.44° in Figure 6a. The insert gives details of the pattern for different values of Q. At $Q = 0.65$ Å^{-1}, i.e. very close to the limit value, the diffraction pattern is a broad and large peak. For other Q values, a three peak structure is visible in contrast with the predictions given in Section 2.2. This feature comprises 2 sharp peaks plus a broad one placed not in the middle of the angular interval. This unexpected supplementary peak is a resolution effect as it disappears when the resolution volume is constrained to be very small and isotropic. When Q increases, going away from the limit value, the angular interval increases and the peaks intensity decreases, accordingly. Figure 6b displays the Q dependency of the different peak positions, which can be calculated by a convenient geometrical model (continuous curves). The tube lattice signal can be parametrized and subtracted from the total signal, giving the C_{60} 1D crystal response alone, the integrated intensity of which has been plotted as function of Q in Figure 6b.

The constant Q scan method presented here allows to separate very simply the contribution from the tube lattice to the one originating from the C_{60} 1D crystal in the diffraction diagram. This can help when one is interested in fine refinement of the structural parameters of the C_{60} chain.

4 Discussion

In this section, we discuss the case of an imperfect 2D oriented peapod sample, similar to usual real samples that are studied by X-ray diffraction. As for the 1D oriented sample, four effects have to be considered: i) dispersion of the parameter; ii) short C_{60} chains; iii) mosaic (also called out of plane mosaic); and iv) correlation between C_{60} chains within the bundles. To quantify the different effects we have to determine the characteristic widths of the convenient Gaussian distributions. As the situation is rather more complex than for the 1D sample we limit the discussion to some examples.

i) Dispersion of the parameter or ii) presence of short chains results in a broadening of the (M) planes, so that each plane presents some thickness (see ii) and iii) in Fig. 3). The only difference between the two cases is that the thickness — or the FWHM of the distribution — keeps the same value for all the $(00l)$ planes in the case of finite size induced broadening, whereas it is multiplied by the index l for a dispersion of lattice parameter as was explained in Section 2. The most favorable configuration for probing these effects is the longitudinal Oy scan (i.e. "$\theta/2\theta$"). In Figure 7a the diffraction pattern calculated for a parameter distribution of $\delta d = 0.53$ Å centered around $d = 9.7$ Å is compared to the case of a perfect sample. The peak at 0.65 Å^{-1} is wider but it remains asymmetric. If we make the assumption that the full line is an experimental result, one can try to extract the parameter dispersion directly by performing a convolution of the perfect sample curve (dash line) by a Gaussian function, the width of which gives the width of the distribution. One gets a δQ value of 0.032 Å^{-1}, for the Gaussian width, which gives a $\delta d = 0.47$ Å using the relation $\delta d/d = \delta Q/Q$. The good agreement between the injected width and the one used doing the convolution makes this method very powerful since with this direct method there is no need to perform a full model calculation. One just has to modelize the diagram for a perfect sample. According to the previous comments, the curve in Figure 7a can also be interpreted with a short chain model. In that case the length of the chain would be $L \sim 2\pi/\delta Q \sim 170$ Å (∼18 C_{60} molecules).

iii) The most convenient configuration to study the out of plane mosaic is a constant Q scan across the Oz axis. In that case the other effects will not interfere with the mosaic effect and the mosaic angle can be determined directly from the signal of the tube lattice. Figure 7b compares the signal originating from the tube lattice for a 4° mosaic sample to that of a perfectly 2D oriented sample (constant Q scan). The effect of out of plane mosaic on the C_{60} crystal signal is also represented on a magnified scale. The two sharp peaks broaden dramatically as soon as the mosaic angle is larger than ∼4°. The magnitude of this effect increases with the distance to the (M) plane $(Q-Q_0)$, where Q_0 is the limit value ($Q_0 = 2\pi/\mathrm{d}$). Interestingly the effect of mosaic on 2θ scans in transmission geometry ($\omega = 0°$) is very different from that of parameter dispersion and short chains. It can be viewed in Figure 7c that the peak at 0.65 Å^{-1} remains sharp even for a mosaic angle as large as 40°, in contrast to the other effects.

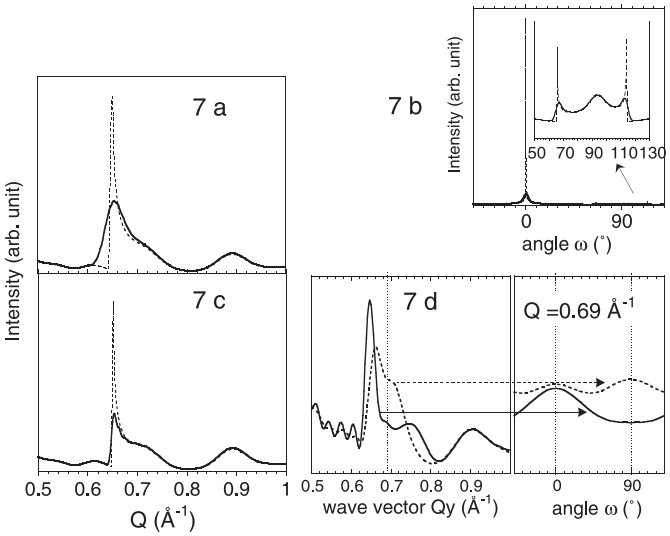

Fig. 7. Imperfect 2D oriented sample. (a) Longitudinal scan along Oy (see Fig. 4) in the case of parameter dispersion or short chains. (b) Effect of the mosaic on constant Q scan at $Q = 0.71$ Å^{-1}, dashed line for perfect sample, continuous line for 4° mosaic. The array of tubes gives the signal around $\omega = 0°$ and the C_{60} signal (inset) is around 90°. (c) Effect of mosaic on "2θ" scans in transmission for a mosaic of 40° (mosaic: continuous line, perfect sample: dashed curve). (d) Scans along Oy and constant Q scan for correlated chains (continuous line) and uncorrelated ones (dashed line). The mosaic angle is 60°.

iv) The experimental determination of the correlation length between C_{60} chains using diffraction patterns is not straightforward. Scans along the (M) planes crossing the Oy axis would allow to measure the corresponding width (see Figs. 4a and 4b). However form factor, mosaic effects and correlations between chains altogether produce a signal decreasing, so that both effects have to be taken into account simultaneously in the interpretation of the data. Nevertheless constant Q scans as described previously will bring pertinent information on this question. Since it is possible to remove the tube lattice response, it would be possible to determine the persistence or the disappearance of the C_{60} chain signal when going away from the Oy axis by successive Q increasing constant Q scans. If 3D correlation exist, the C_{60} crystal response in Figure 6a will rapidly disappear as soon as Q departs from $Q_0 = 2\pi/d$.

In Figure 7d we simulate a longitudinal scan along Oy (see Fig. 4) for a very large out of plane mosaic of 60° (FWHM) in the case of strongly correlated C_{60} chains (continuous curve) and chains with no correlation (dashed curve). For the second curve the amplitude is displaced toward the high Q side of the (001) peak. We also simulate constant Q scans at $Q = 0.69$ Å^{-1} in Figure 7d (right). Due to the large out of plane mosaic the narrow peak at $\omega = 0°$ in

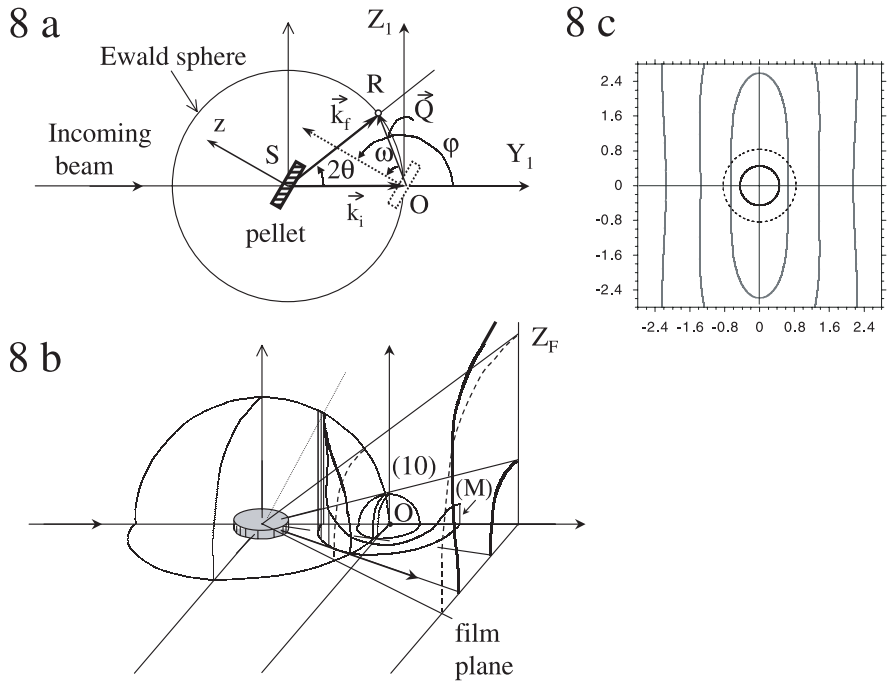

Fig. 8. Ewald construction and its application to an image plate configuration. (a) Ewald construction in a plane and definition of the angles φ and ω. (b) Application to the image plate method; the pellet is horizontal, at the center of the sphere. The reciprocal space is plotted at point O. (c) Film plane; the small circle is the (10) reflection, the dashed line circle is a constant Q scan, the other continuous lines are the images of the cylinders related to the different (M) planes (Fig. 4a).

Figure 7b transforms into a very broad one centered at 0°. As it corresponds to the crossing of the Oz axis this peak is due to the 2D lattice. In a similar way the 3 peaks structure corresponding to the crossing of the (M) plane (inset of Fig. 7b) becomes a very broad peak centered at $\omega = 90°$ (see dashed curve in Fig. 7d right). This constant Q scan proves that the 1D C_{60} crystal presents a strong contribution to the signal for chains with no correlation whereas it is very small for correlated chains. This example illustrates the method used to separate the 1D and 2D contributions using constant Q scans.

Finally we make a comment about the frequently used diffraction experiments of 2D oriented peapods using an image plate as detector [12]. The Ewald construction for this experiment is represented in Figure 8b and a schematic description of the result in the film plane is shown in Figure 8c. This method operates in a "2θ" mode: each line of the film going through the center is a "2θ" scan as described above. Each circle on the film is a kind of constant Q scan (dashed lines in Figs. 8b and 8c). One remarks that constant Q scans performed with this film method are different from those described previously as they do not intercept the Oz axis (see the C line in Fig. 4a). In the geometry represented in Figure 8b the (hk) reflections of the tubes lattice appear as circles on the plane of the image plate (Fig. 8c). The cylinders representing the small Q limit of the (M) planes cut the Ewald sphere along lines that appear as curves with a vertical peanut shape onto the film plane. This figure does not take into account the intensity along the curve but only the positions. The (hk) reflections give a large intensity along the vertical axis and the $(00l)$ (M) planes responses are strong along the horizontal axis. The corresponding "2θ" scans are shown in Figure 9. As the vertical scan ends up at 1.8 Å^{-1} the first (M) plane contribution does not appear and only (hk) reflections are visible (the first (M) plane signal would be at 2.4 Å^{-1}). On contrary the (001) and (002) signals are strong in the horizontal scan. This method is powerful for a very good approximation of

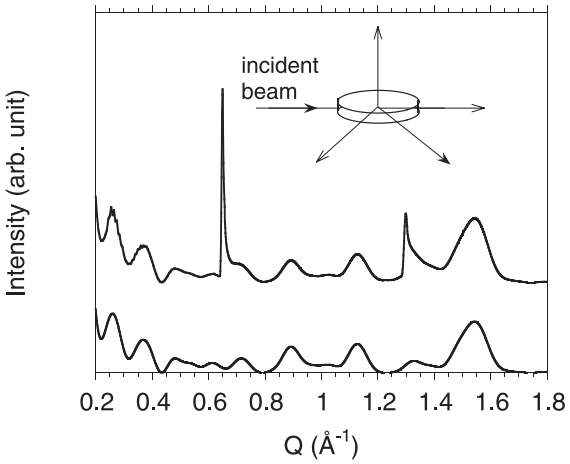

Fig. 9. Schematic results of the image plate method: the upper curve is a scan along the horizontal line of the film, the lower curve is for the vertical one.

the C_{60}–C_{60} distance, even with a large out of plane mosaic sample (see Sect. 3.2). Making a difference curve by combining these two curves according to some convenient weighting is a way to remove almost completely the 2D signal, thus enhancing the 1D signal [12].

In summary, we have performed a theoretical investigation of the diffraction diagram of oriented samples of peapods. Different cases of the orientation, from perfectly 1D oriented samples to imperfect 2D oriented pellets were taken into account. We have shown that using appropriate scans according to the sample symmetry, i.e. longitudinal scans along the symmetry axis of the pellet (or of the fiber) and in a direction perpendicular to this axis, it is possible to get a number of pertinent informations on the structure of the peapods. In all cases the constant Q method (along the C line) permit to distinguish between the 2D (lattice) and the 1D (C_{60}) contribution, even in unfavorable cases where the out of plane mosaic is as large as 60°. Concerning the polymerization state of C_{60} molecules, longitudinal scans are the more convenient to determine the C_{60}–C_{60} distance. A further step inside the knowledge of the system would be to determine the correlation length along the chains and finally the last step would be to modelize these results by the appropriate distribution of monomers, dimers and polymers. Concerning the correlation state between chains we have described a convenient method (see Fig. 7d) that allows to probe such correlation even for samples showing a large out of plane mosaic. Finally we remark that these different methods apply also to fibers provided that the sample orientation presents a cylindrical symmetry axis.

Appendix A

A.1 Ewald sphere and definition of the ω and φ angles

The wave vectors of incoming and diffracted beams, $\boldsymbol{k_i}$ and $\boldsymbol{k_f}$ are related to the wavevector $\boldsymbol{Q}$ by (see Fig. 8a):

$$\boldsymbol{k_f} = \boldsymbol{k_i} + \boldsymbol{Q} \text{ and } k_f = k_i = \text{Ewald sphere radius.}$$

The sample is at the center of the Ewald sphere S. The reciprocal space of the sample is drawn at point O which is the origin of $\boldsymbol{Q}$. The orientation of the pellet is given by the angle φ. One has: $\varphi = 90 + \theta + \omega$. At $\varphi = 0$ or 180° the pellet is perpendicular to $\boldsymbol{k_i}$ (transmission geometry). At $\omega = 0$ the normal to the pellet is parallel to $\boldsymbol{Q}$ (reflection geometry). The signal is collected at the end of $\boldsymbol{Q}$, at point R, which is the center of the resolution volume.

A.2 Ewald sphere in 3D space in the case of an horizontal pellet (Fig. 8b)

The signal collected on the film corresponds to the response lying on the Ewald sphere surface and delimited by a convenient solid angle associated to the film surface. The figure is made for an horizontal pellet. In Figure 8c a schematic representation of the result is indicated. In a real experiment the scales depend on the sample to film distance. We preferred to use a scale in $Å^{-1}$, i.e. in reciprocal space in Figure 8c.

References

1. S. Iijima, Nature (London) **354**, 56 (1991)
2. X. Liu, T. Pichler, M. Knupfer, M.S. Golden, J. Fink, H. Kataura, Y. Achiba, K. Hirahara, S. Iijima, Phys. Rev. B **65**, 045419 (2002)
3. M. Monthioux, Carbon **40**, 1809 (2002)
4. B.W. Smith, M. Monthioux, D.E. Luzzi, Chem. Phys. Lett. **315**, 31 (1999)
5. A. Gloter, K. Suenaga, H. Kataura, R. Fujii, T. Kodama, H. Nishikawa, I. Ikemoto, K. Kikuchi, S. Suzuki, Y. Achiba, S. Iijima, Chem. Phys. Lett. **390**, 462 (2004)
6. M. Abe, H. Kataura, H. Kira, T. Kodama, S. Suzuki, Y. Achiba, K. Kato, M. Takata, A. Fujiwara, K. Matsuda, Y. Maniwa, Phys. Rev. B **68**, 041405(R) (2003)
7. J. Cambedouzou, S. Rols, R. Almairac, J.-L. Sauvajol, H. Kataura, H. Schober, Phys. Rev. B **71**, 041403(R) (2005)
8. S. Kawasaki, Y. Matsuoka, T. Yokomae, Y. Nojima, F. Okino, H. Touhara, H. Kataura, Carbon **43**, 37 (2005)
9. The C_{60}–C_{60} distance obtained from electron diffraction (Ref. 12) is sligthly higher than the distance obtained from X-ray diffraction
10. F. Cui, C. Luo, J. Dong, Phys. Lett. A **327**, 55 (2004)
11. J. Cambedouzou, V. Pichot, S. Rols, P. Launois, P. Petit, R. Klement, H. Kataura, R. Almairac, Eur. Phys. J. B **42**, 31 (2004)
12. W. Zhou, K.I. Winey, J.E. Fischer, T.V. Sreekumar, S. Kumar, H. Kataura, Appl. Phys. Lett. **84**, 2172 (2004)
13. X. Liu, T. Pichler, M. Knupfer, J. Fink, H. Kataura, Phys. Rev. B **69**, 075417 (2004)
14. N. Bendiab, R. Almairac, J.-L. Sauvajol, S. Rols, E. Elkaim, J. Appl. Phys. **93**, 1769 (2003)